Journal of Materials Chemistry A

ROYAL SOCIETY OF CHEMISTRY

PAPER

View Article Online
View Journal | View Issue

Cite this: J. Mater. Chem. A, 2023, 11, 17828

Elucidating the lithium deposition behavior in open-porous copper micro-foam negative electrodes for zero-excess lithium metal batteries†

Tjark T. K. Ingber, [a] Marlena M. Bela, [a] Frederik Püttmann, [a] Jan F. Dohmann, [a] Peter Bieker, [b] Markus Börner, [a] Martin Winter [ab] and Marian C. Stan *[ab]

In zero-excess lithium metal batteries (ZELMBs), also termed "anode-free" LMBs, Li from the positive electrode is electrodeposited onto a bare current collector instead of the Li metal negative electrode commonly used in LMBs. This enables high theoretical energy density and facile, safe, and low-cost assembly. To tackle coulombic inefficiencies during Li deposition/dissolution, 3D structured current collectors can be used instead of 2D foil materials. This study elucidates the Li deposition behavior in custom-made open-porous Cu micro-foams from nucleation to large scale deposition. For the first time in ZELMBs, surface and sub-surface Li deposits in open-porous 3D materials are compared to deposits on 2D foils using cryogenic focused ion beam scanning electron microscopy (cryo-FIB-SEM). The results highlight that Cu micro-foams can store substantial amounts of dendrite-free Li in their open-porous 3D structure, minimizing detrimental volume changes during Li deposition/dissolution. Electrochemical analyses and simulations reveal that current density distribution over the large surface area of the Cu micro-foams reduces the Li nucleation overvoltage by ≈40%. Also, charge/discharge cycling in ZELMBs shows increases in coulombic efficiency, capacity retention, and cycle life. Overall, this work explains how open-porous Cu micro-foam current collectors improve the Li deposition behavior to boost the cycling characteristics of ZELMBs.

Received 10th July 2023
Accepted 2nd August 2023

DOI: 10.1039/d3ta04060g

rsc.li/materials-a

Introduction

The rapid evolution of modern-day electrically powered mobile applications in private and industrial sectors calls for ever increasing battery performance.[1–5] Lithium metal battery (LMB) concepts that utilize a Li metal negative electrode and a transition metal layered oxide-based positive electrode are among the most promising high energy battery set-ups to date.[6–10] Serving as a reservoir to replenish Li losses during operation, the Li metal in LMBs is often referred to as the Li excess in relation to the positive electrode, since the bulk Li is not initially involved in charge/discharge cycling.[11] In order to maximize the specific energy and energy density of LMBs, current developments aim to continuously decrease the Li excess to achieve lower weight and volume.[4,12–14] This trend leads to cells with only a thin current collector and no Li metal at the negative electrode which are referred to as zero-excess LMBs (ZELMBs) or anode-free LMBs. In these cells, the Li content included in the positive electrode upon cell assembly constitutes the total electrochemically active Li inventory of the cell, thus eliminating any Li excess.[10,15–19] ZELMBs possess several key advantages compared to their counterparts with Li metal negative electrodes, including higher safety in pristine state, lower cost, and ease of assembly. Also, they deliver increased estimated stack level specific energy (420 W h kg^{-1}) and energy density (1288 W h L^{-1}) values with organic carbonate-based liquid electrolytes (details in Table S1, ESI†).[4,18–21] Comparable LMB cells with a Cu current collector-based thick Li metal negative electrode deliver lower estimated stack level specific energy and energy density values of only 376 W h kg^{-1} and 770 W h L^{-1}, respectively (Table S1†).[4] A further advantage of ZELMBs is that they can serve as a model system to generate insights about the cycling behavior of Li by revealing undesirable Li loss, which could otherwise be masked by replenishment with excess Li.[18]

However, the operation of ZELMBs is still characterized by fast capacity fading due to severe losses of Li inventory upon charge/discharge cycling.[21,22] These losses stem from the formation of solid electrolyte interphases (SEI) through reactions between the Li metal and the liquid electrolyte.[21–24] Moreover, the inhomogeneity of the Li deposition/dissolution causes the growth of high surface area Li (HSAL) such as Li

[a]MEET Battery Research Center, University of Münster, Corrensstraße 46, 48149 Münster, Germany. E-mail: marian.stan@uni-muenster.de

[b]Helmholtz-Institute Münster, IEK-12, Forschungszentrum Jülich GmbH, Corrensstraße 48, 48149 Münster, Germany. E-mail: m.stan@fz-juelich.de

† Electronic supplementary information (ESI) available. See DOI: https://doi.org/10.1039/d3ta04060g

dendrites that expose fresh Li surfaces to the electrolyte, inciting further Li-consuming SEI formation. After repeated cycling, the individual HSAL protrusions can get isolated from the electrode surface, which leads to further Li loss through the formation of electrochemically inactive "dead" Li.[21–26] Another detrimental factor is the recurrent volume fluctuation because of the frequent electrochemical deposition and redissolution of the temporary Li metal layer. This fluctuation causes mechanical stress that can wear down cell components, reducing the cycle life of the battery.[23,27,28] The continuous loss of Li inventory is expressed by a low coulombic efficiency (CE), particularly in the initial cycles.[21]

To achieve increased CEs and a prolonged cycle life for ZELMBs, a homogeneous and reversible Li charge/discharge behavior and reduced decomposition reactions in the cell are desirable.[21] In this regard, a lot of attention has been devoted to the electrolyte design[29–37] and optimized cycling conditions for ZELMBs,[18,24,38] as well as functional coatings and surface modifications for the negative electrode.[27,39–46] Table S2 (ESI†) summarizes the capacity retention improvements that were achieved in several recent studies using ZELMBs with optimized Cu-based negative electrode substrates. For example, a remaining capacity of 80% after 120 cycles was reported for a ZELMB with a Si/polyacrylonitrile-coated Cu negative electrode.[47] Further research has also been directed towards the use of non-planar current collectors such as patterned materials and porous media as substrates for Li deposition.[46,48–52] These concepts focus on using 3D materials that provide internal spaces for Li deposition instead of the conventionally used 2D foil substrates, potentially preventing volume and pressure fluctuation as well as Li dendrite growth.[48,50,53]

The array of techniques available to produce suitable porous materials ranges from processes based on thermal treatments[54,55] or alloying and dealloying reactions[56–59] to deposition methods such as chemical vapor deposition (CVD)[60,61] and electrodeposition.[62–64] For instance, Umh *et al.* prepared a highly porous dendritic Cu superstructure that enabled a reversible uptake of Li with a CE of 95% for 140 cycles in cells with Li metal negative electrodes.[64] Other examples include a foam-like electrode structure based on carbon black and $LiNO_3$ particles,[65] as well as a high dielectric 3D-scaffold material applied on a conductive base layer to guide the bottom-up Li deposition and suppress dendrite growth.[66] These approaches proved to notably boost the performance of cells with Li metal or layered oxide-based electrodes as the Li source by effectively homogenizing Li metal deposition. While these studies demonstrate the potential of porous negative electrode substrates in ZELMBs, the presented 3D materials offer little control of their porosity parameters, and detrimental volume fluctuations during deposition and dissolution of Li metal remain largely unregulated. Furthermore, the Li deposition behavior in the internal volume of the demonstrated 3D media was not investigated in detail, which highlights a notable gap in current ZELMB research.

To address this shortcoming, the present study focuses on a detailed investigation of the Li deposition behavior in an electronically conductive open-porous current collector for ZELMBs. Expanding upon the literature reports mentioned above, a thorough understanding about where and how exactly Li metal can be stored in the 3D structure is provided. Suitable Cu micro-foams, not before used in a ZELMB set-up, were produced using an optimized templated electrodeposition process that was developed from elements of studies on micro-particle generation[67–69] and inverse opal structures.[70–72] For the first time in a ZELMB set-up, *in situ* scanning electron microscopy analysis of cross-sections prepared by cryogenic focused ion beam milling (cryo-FIB-SEM) was used to elucidate the initial stages of internal Li deposition behavior in an open-porous micro-foam material. The cryo-FIB-SEM results are combined with top-view SEM, X-ray photoelectron spectroscopy (XPS), current density distribution simulation, and electrochemical analysis. This provides a new perspective that reveals, in which way the use of porous 3D materials in ZELMBs can enable a more homogeneous Li deposition that best utilizes the internal void spaces of the host structure. This also reduces the issue of volume expansion as compared to conventional 2D deposition substrates. While prior works mostly focused on demonstrating electrochemical cycling improvements and depicting large-scale Li deposition, the present study provides more detailed insights into the beneficial effect of porous current collectors on early Li metal deposition in ZELMBs. This expands the current state of understanding, underlining the significance of the current collector morphology in the ZELMB cell set-up.

Experimental

Materials

Polyvinyl alcohol (PVA, 87–90% hydrolyzed), acetone, sulfuric acid (H_2SO_4, 96%), copper sulfate pentahydrate ($CuSO_4 \cdot 5H_2O$, 99%), lithium difluoro(oxalato)borate (LidFOB, 99%), and lithium tetrafluoroborate ($LiBF_4$, 99.99%) were obtained from Sigma-Aldrich, USA. Polylactic acid (PLA) was supplied by GoodFellow, UK. Dichloromethane (DCM) was obtained from Carl Roth, Germany. Ethanol was bought from AppliChem, Germany. Flat and dendritic Cu foils (50 μm thickness) were supplied by Carl Schlenk, Germany. Li foil (500 μm thickness) was obtained from Honjo Chemical Company, Japan. $LiNi_{0.8}Co_{0.15}Al_{0.05}O_2$ (NCA) was supplied by Targray Technology International, Canada. Diethyl carbonate (DEC) and fluoroethylene carbonate (FEC) were obtained from BASF, Germany. The Cu foils were rinsed with diluted hydrochloric acid, ethanol, and water before use. All other materials were used as received without further purification.

Preparation of Cu micro-foams

Cu micro-foams were prepared by electrodeposition of Cu at a polymer micro-particle template. Micro-particles of PLA were synthesized using an emulsion solvent evaporation approach that was developed and optimized based on studies by Zatorska *et al.*,[67] Jalil *et al.*,[68] and O'Donnell *et al.*[69] PVA (12 g) was dissolved in deionized water (600 mL) by vigorously stirring at 60 °C for 24 hours in a closed flask. The remaining undissolved

residues were filtered off from the solution. PLA (300 mg) was dissolved in DCM (50 mL). The PLA solution was added dropwise to the PVA solution under vigorous stirring to create small, dispersed droplets. The mixture was heated to 50 °C and stirred for 24 hours in an open flask. After complete evaporation of the DCM, the resulting dispersion was centrifuged to separate white PLA micro-particles that have been released from the evaporating DCM droplets. The particles were washed with deionized water and ethanol and dried at 40 °C at reduced pressure.

PLA micro-particles (10 mg) were dispersed in a mixture of acetone (50 μL) and ethanol (20 μL) by vortex mixing. The dispersion was drop-cast onto a Cu foil disk (15 mm diameter) and left to dry. To ensure adherence to the base Cu foil and a slight coalescence of the PLA particles, the coated Cu disk was sintered in a glass furnace at 200 °C for 20 minutes under argon atmosphere after evacuation to exclude residual oxygen. After cooling down, the disk was wetted with a small droplet of ethanol (10 μL). To be used as the working electrode of a three-electrode electrodeposition set-up, the sample was placed in a $CuSO_4$ solution (0.6 M) made by dissolving $CuSO_4 \cdot 5H_2O$ (9.57 mg) in deionized water (100 mL) and 1 M H_2SO_4 (0.5 mL). The counter electrode was a sheet of Cu foil and the reference electrode was Ag|AgCl. A Solarton Galvanostat/Potentiostat SI1287A (Ametek Scientific Instruments, USA) was used for electrodeposition of Cu in the spaces between the particles of the PLA template. Potentiostatic deposition at 200 mV was executed for 80 minutes, which was determined to be the optimal deposition time to completely fill the voids without causing spillover Cu deposition ("plating") on top of the template. After the deposition, the sample was washed with deionized water and DCM before sonicating it in DCM for 30 minutes to achieve full removal of the PLA template, revealing an open-porous Cu micro-foam structure supported on the base Cu foil disk.

Cell assembly

The electrodeposited Cu micro-foam samples were punched into circular electrodes with a diameter of 12 mm. To investigate the Li deposition morphology occurring during a single deposition step, two-electrode coin cells (CR2032) were assembled using either the prepared Cu micro-foam electrodes or equivalent Cu foil disks as the positive electrode and Li foil disks (12 mm diameter) as the negative electrode. For the continuous electrochemical charge/discharge experiments, flat Cu foil, dendritic Cu foil, or Cu micro-foam disks were used as the negative electrodes in coin cells with circular NCA-based positive electrodes (95% NCA, 3% conductive carbon, 2% poly(vinylidene difluoride) (PVdF) binder, 1.00 mA h cm^{-2} areal capacity, 5.3 mg cm^{-2} areal coating mass, 15.3 μm coating thickness, 188 mA h g^{-1} specific capacity, 12 mm diameter) on Al current collectors. In all cells, two layers of polyolefin nonwoven (Freudenberg FS2190) sandwiched between two layers of polypropylene monolayer membranes (Celgard 2500) were used as the separator stack. The electrolyte for the deposition morphology investigations was composed of 1 M LidFOB and 0.2 M $LiBF_4$ in a mixture of diethyl carbonate (DEC, BASF) and fluoroethylene carbonate (FEC, BASF) with a ratio of 2 : 1 by volume as proposed by Weber *et al.* as a suitable electrolyte composition for ZELMBs.[34] For the deposition voltage investigations and the charge/discharge cycling experiments, the salt contents in the electrolyte were doubled (2 M LidFOB and 0.4 M $LiBF_4$). Cell assembly was performed in an argon-filled glovebox with H_2O and O_2 contents constantly below 1 ppm.

Morphological and spectroscopical investigations

Surface and cross-section SEM images were acquired using an AURIGA scanning electron microscope (Carl Zeiss Microscopy, Germany) at an accelerating voltage of 3 kV. Focused ion beam (FIB) milling was performed using an Ion-sculptor FIB column (Carl Zeiss Microscopy) at an acceleration voltage of 30 kV and milling currents of 30 nA for primary milling and 15 nA for polishing. For Li containing samples, a cryo-FIB stage was employed to execute the milling at −160 °C to avoid effects that could change the deposited Li morphology.

Determination of material volume and density *via* helium (He) pycnometry was done using an AccuPyc II 1340 device (Micromeritics Instrument Corporation, USA). Each measurement was executed over 30 cycles with an equilibration rate of 0.005 psig min^{-1}.

X-ray photoelectron spectroscopy (XPS) was carried out using an Axis Ultra DLD spectrometer (Kratos Analytical, UK) equipped with an Al K_α source (1486.6 eV). Measurements were conducted at a filament voltage of 12 kV, a filament current of 10 nA and a detector pass energy of 20 eV. For sputter depth profiling, a monoatomic Ar ion beam with an acceleration voltage of 4 kV was applied between the measurements. CasaXPS 2.3.24 software was used for data evaluation.[73]

Current density distribution simulation

Structure modelling and simulations of current density distributions were carried out using COMSOL Multiphysics 5.5 software including the "Batteries & Fuel Cells Module". Square sheets of flat and dendritic Cu foil (21 μm side length) and an open-porous Cu micro-foam ($x = 21$ μm, $y = 21$ μm, $z = 20$ μm) were modelled as negative electrode substrates. An equal current of 0.1 mA cm^{-2} relative to the geometric area in the x–y-plane was applied to all models. The distribution of the applied current over the models was simulated for a ZELMB set-up with a transition metal layered oxide-based positive electrode and an organic carbonate-based liquid electrolyte.

Electrochemical characterization

For electrochemical characterization, the cells were connected to a MACCOR 4000 battery testing unit (MACCOR, USA) using a temperature control chamber (Binder, Germany) at 40 °C. All current densities and charging capacities are given with respect to the electrodes' geometric surface area in the x–y-plane, disregarding any porosity. To investigate the Li deposition morphology, Cu||Li cells with Cu foil or Cu micro-foam as the positive electrode were first rested for 12 hours. Li amounts equivalent to 0.05, 0.20 or 1.00 mA h cm^{-2} were deposited at a current rate of 0.1 mA cm^{-2}. The cells were opened, and the

Cu substrates were retrieved and dried for SEM analysis. For electrochemical charge/discharge experiments, cells with flat Cu foil, dendritic Cu foil, or Cu micro-foams as the negative electrodes and NCA-based positive electrodes were prepared and rested for 12 hours before operating them in a voltage range of 3 V–4.3 V at a current density of 0.2 mA cm^{-2} (0.2C) for 100 cycles. For every cycling experiment, the results of three equivalent cells were averaged. Out of these three cells, the most representative one was chosen for depiction of the charge/discharge voltage curves. CE values were calculated as the ratio between discharging and charging capacity for a given cycle.

Results and discussion

Characterization of the Cu micro-foams

The process used to fabricate open-porous Cu micro-foam samples by electrodeposition of Cu onto a base layer after templating with self-synthesized PLA micro-particles is schematically depicted in Fig. 1a. The synthesized open-porous Cu micro-foam structures were analyzed *via* SEM and the results are displayed in Fig. 1b–d. During the electrodeposition of Cu onto the templated base layer as presented in Fig. 1a (step V), the voids between the PLA micro-particles of the template were filled up with metallic Cu as marked in yellow in Fig. 1b. After removal of the PLA micro-particles, the remaining Cu skeleton represents the "negative" of the originally assembled deposition template, inheriting all its structural features. Fig. 1c shows the finished open-porous Cu micro-foam material. The temperature treatment of the PLA template before the electrodeposition led to a slight coalescence of the micro-particles. This widened the necks of the connecting channels between the spherical pores, resulting in a spacious open morphology of the pore network. The inner pore walls are smooth and uniform while the top ending of the solid Cu compartments feature a rough appearance that is characteristic of Cu electrodeposited from the used electrolyte bath (Fig. S1a, ESI†).

Characterization of the bulk pore distribution was enabled by FIB-preparing a cross-section of a Cu micro-foam. The corresponding SEM image in Fig. 1d shows that the top of the micro-foam structure is covered with a protective Pt coating (marked in blue) applied prior to the FIB milling to facilitate a smooth cutting edge. The cross-section image confirms that the bulk micro-foam structure (marked in green) features a large number of interconnected open pores that create substantial internal void spaces. The plane where the Cu micro-foam is grown on top of the base Cu layer (marked in orange) is clearly visible, indicating a good adherence of the Cu micro-foam to the Cu foil. The open-porous structure features uninterrupted pathways from the top surface down to the lowest pores that render the entirety of the pore network accessible for liquid electrolytes. Also, the high electronic conductivity of Cu provides high electron availability throughout the micro-foam, which is essential for long-term charge/discharge cycling.

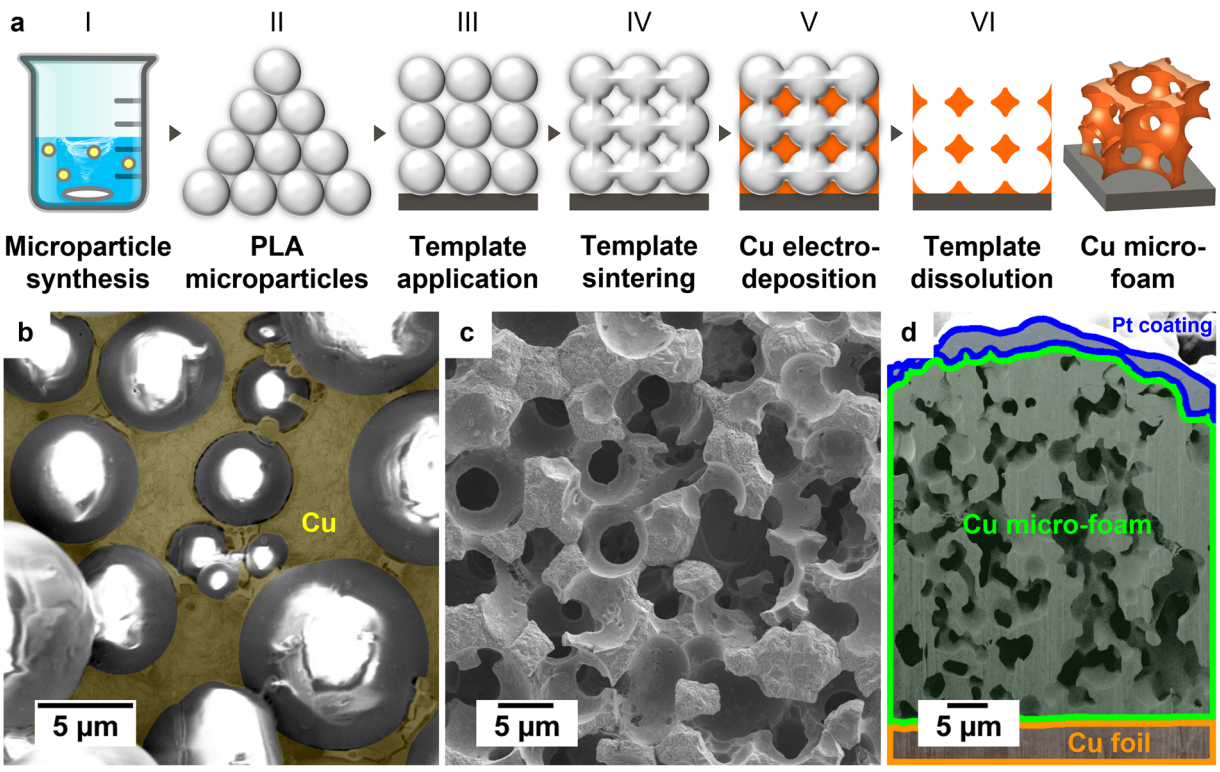

Fig. 1 (a) Stepwise depiction of the process used to fabricate the Cu micro-foams. Surface SEM images of the fabricated Cu micro-foam material (b) before and (c) after the removal of the PLA template. (d) Cross-section SEM of the Cu micro-foam after sample preparation using FIB. Yellow area in (b) represents the electrodeposited Cu. Color coding in (d): Cu foil base layer = orange, Cu micro-foam = green, protective Pt coating layer = blue.

Using the preparation method presented herein, the pore size of the Cu micro-foam material is adjustable by tuning the size of the template PLA particles. Literature studies suggest that pore diameters for 3D deposition substrates should be larger than 1 μm to offer enough space for Li deposition inside the porous volume, counteracting extensive surficial deposition and limiting dendrite growth. On the other hand, too generous pore sizes lead to pore walls resembling a flat electrode surface that offers limited mechanical support and electrical contact, preventing effective control of the Li deposition morphology.[50,74,75] The pore sizes in this work are ≈5 μm which fits well with optimal pore diameters identified in previous studies.[50,75] The average thickness of the Cu micro-foam material excluding the Cu foil base layer is 52.2 μm ± 9.4 μm. Based on He pycnometry measurements, the average porosity of the Cu micro-foams was determined to be 71.2% ± 4.4%. This results in a theoretical areal capacity of 7.66 mA h cm^{-2} ± 1.38 mA h cm^{-2}, assuming complete Li metal filling of the Cu micro-foam pores. Calculations according to Faraday's law predict an average Cu micro-foam thickness of 76.9 μm ± 11.2 μm based on the determined porosity and the amount of charge transmitted during the electroplating process. Comparing this prediction to the measured thickness implies an average efficiency of 67.9% for the aqueous Cu electrodeposition process.

The current density distributions in a simplified model of the prepared Cu micro-foam and in flat Cu foil were comparatively simulated with COMSOL Multiphysics. An equal current of 0.1 mA cm^{-2} relative to the geometric *x*–*y*-plane area was applied to both models. While Fig. 2a shows an entirely homogeneous current density of 0.1 mA cm^{-2} on the flat Cu foil surface, the effective current density distribution in the open-porous Cu micro-foam is more diverse. Fig. 2b reveals that the current density on the top surfaces and in the surface pores of the Cu micro-foam model is mostly below 0.1 mA cm^{-2}. Further down along the *z*-axis, the current density increases continuously until values higher than 0.7 mA cm^{-2} are reached in the lowest pores. This progression is more clearly visualized by three horizontal slices from the micro-foam model that represent the top surface of the micro-foam as well as pore walls in the middle and lower area of the model. Despite the simplified character of the presented simulations, these results clearly show that the effective current density on the top surfaces of the micro-foam is considerably lower than that on a flat Cu foil. On the other hand, the current density on some parts of the pore walls further down from the surface can be higher than the reference value.

Li deposition at Cu micro-foams

To evaluate the Li deposition properties during electrochemical cycling in ZELMBs, amounts of Li equal to 0.05 mA h cm^{-2}, 0.20 mA h cm^{-2}, and 1.00 mA h cm^{-2} were electrodeposited onto the produced Cu micro-foams and flat Cu foil. The applied deposition current represented a current density of 0.1 mA cm^{-2} relative to the geometric *x*–*y*-plane area of the electrodes, disregarding any porosity. The SEM images in Fig. 3a–d depict the generated Li deposits on the micro-foam surfaces together with a pristine electrode for reference. These results are compared to images of analogous Li deposition amounts on planar Cu foil that are shown in Fig. 3e–h.

Fig. 3 shows that the surface of the Cu micro-foam material is substantially less covered with Li structures as compared to flat Cu foil after deposition of equal amounts of Li. The main reason for this is the possibility of Li deposition occurring inside the pores of the micro-foam in addition to Li plating on the surface, in contrast to Cu foil. At a low deposition amount of 0.05 mA h cm^{-2}, the larger part of the Li is deposited inside the porous structure of the Cu micro-foam (Fig. 3b). Few dense Li structures (marked with red arrows) cover ≈3.7% of the micro-foam surface. On the other hand, Fig. 3f shows that the same electrodeposition process forms a large number of Li structures distributed over the flat Cu foil, covering ≈20.8% of the substrate surface. After deposition of 0.20 mA h cm^{-2} (Fig. 3c) and 1.00 mA h cm^{-2} (Fig. 3d) of Li, ≈7.0% and ≈41.8% of the micro-foam surface are covered by Li structures, respectively. This implies that still most of the Li electrodeposits inside the porous Cu micro-foam network, keeping large portions of the

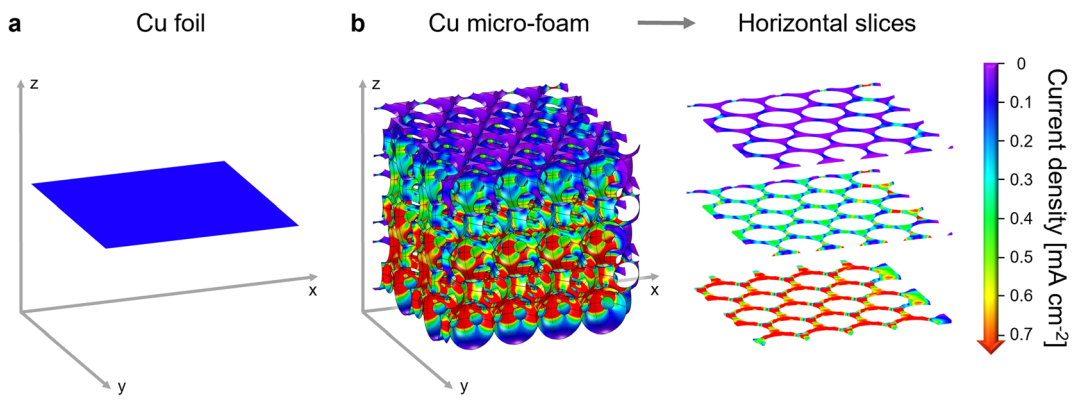

Fig. 2 Current density distribution in (a) flat Cu foil and (b) a simplified model of the Cu micro-foams simulated with COMSOL Multiphysics. An equal current of 0.1 mA cm^{-2} relative to the geometric area in the *x*–*y*-plane was applied to both models. Part (b) contains three horizontal slices from the micro-foam model, depicting the current density distribution in the Cu material at the top surface, at a medium depth, and close to the bottom of the modelled structure. The same color scale was used for all current density visualizations.

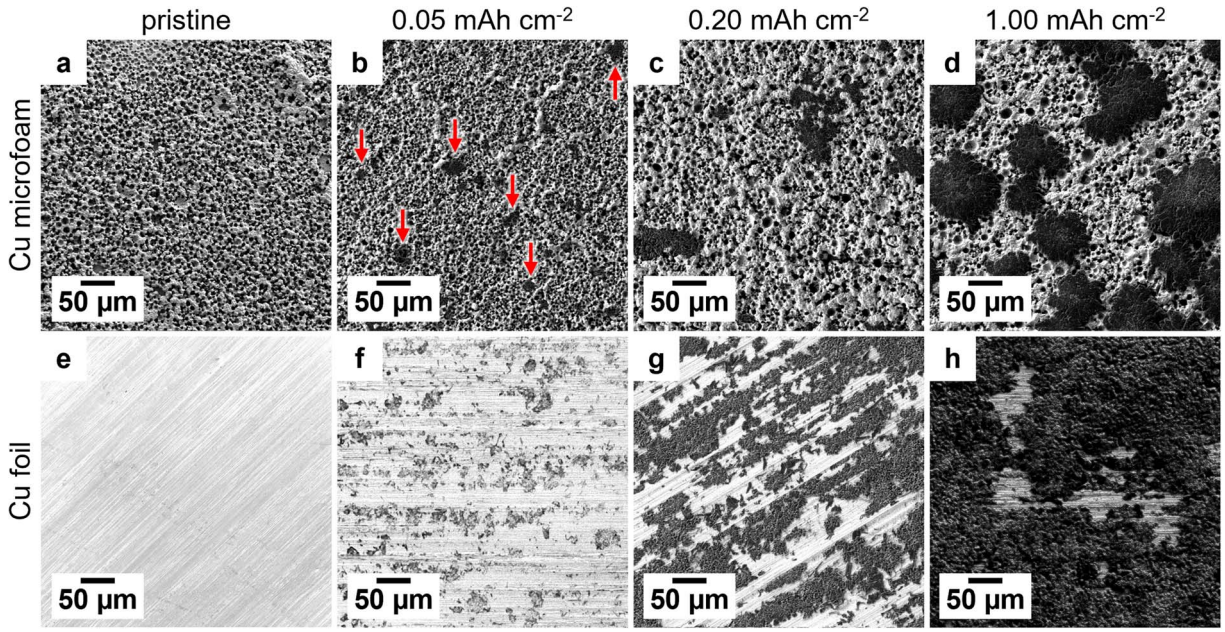

Fig. 3 Pristine (a) Cu micro-foam and (e) Cu foil substrates compared to metallic Li deposited on (b–d) Cu micro-foams and (f–h) Cu foil. Using a current density of 0.1 mA cm^{-2}, Li amounts equal to (b and f) 0.05 mA h cm^{-2}, (c and g) 0.20 mA h cm^{-2}, and (d and h) 1.00 mA h cm^{-2} were deposited. Arrows in (b) mark deposited Li structures.

surface free from discernible Li deposition structures. At the same deposition amounts, the plain Cu foil gets increasingly covered in numerous mossy Li structures of all sizes that occupy ≈59.4% and ≈92.7% of the surface at deposition amounts of 0.20 mA h cm^{-2} (Fig. 3g) and 1.00 mA h cm^{-2} (Fig. 3h), respectively. Although these percentages represent just a rough estimate of the Li distribution based on the visible surface covering in Fig. 3, the morphology of the Cu micro-foam material appears to limit the growth of Li structures on the surface while fostering electrodeposition of Li ions inside the pore structure (see also Fig. S1†).

The Li deposition behavior inside the porous Cu micro-foam was investigated in detail through cryo-FIB-SEM analysis of a sample with 0.20 mA h cm^{-2} of deposited Li. The cross-section SEM image in Fig. 4a shows for the first time that the surface pores in the deposition area are almost completely filled with Li metal (depicted in dark grey) that conforms well to the pore walls. The sub-surface pores also show large Li deposits, highlighting the extensive electrodeposition of Li inside the porous structure of the Cu micro-foam.

Fig. 4a indicates that the large Li structures first seen in Fig. 3 emerged from Li nuclei in surface or sub-surface pores and evolved by growing up towards the micro-foam surface. Due to the low effective current density in the upper pores of the Cu micro-foam where the Li electrodeposition takes place, the expanding and merging Li structures filled the pores in a dense, compact morphology. This led to a high utilization of the free pore volume that minimized remaining internal void spaces. Since most of the Li was deposited inside the pores without outgrowing the porous substrate surface, the electrode

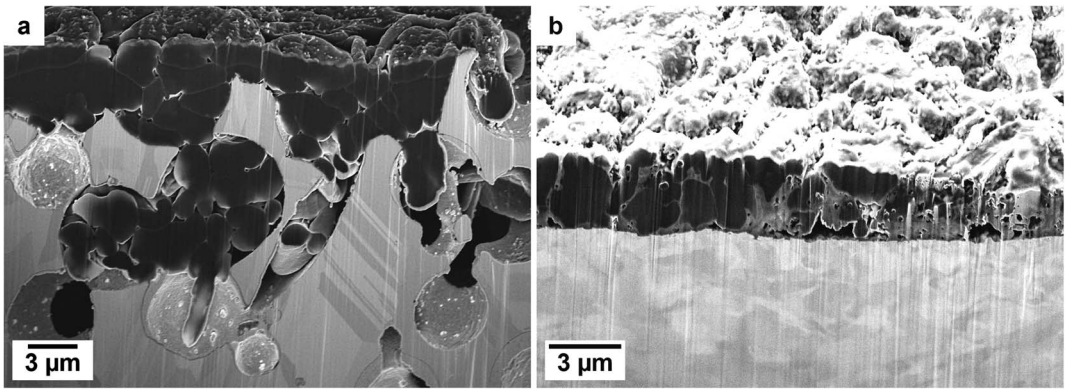

Fig. 4 Cryo-FIB cross-section SEM images of (a) Cu micro-foam and (b) flat Cu foil after electrodeposition of an amount of metallic Li equal to 0.20 mA h cm^{-2} using a current density of 0.1 mA cm^{-2}.

thickness remained similar and the Cu micro-foam effectively mitigated large detrimental volume expansion.

Fig. 4a also shows that the densely growing Li metal tends to block the connecting channels to underlying pores. This prohibits the influx of Li-carrying electrolyte into these pores, preventing Li deposition in them. This growth behavior is the reason for the decreasing amount of deposited Li observed in the pores closer to the bottom of the Cu micro-foam electrode. In addition, the high electronic conductivity of Cu leads to a high electron availability throughout the Cu micro-foam structure. Therefore, Li ions do not travel very deeply into the pore network but rather deposit in a spot close to the surface where they first contact the Cu micro-foam or existing Li structures. Still, the observed deposition mode clearly highlights the advantage of using the porous Cu micro-foams as substrates for Li deposition by considerably reducing the amount of surface deposits, limiting the volume expansion during the electrodeposition process.

The degree of pore filling and the proportion of Li deposited in the pores are also influenced by the effective current density distribution. As discussed above, a larger specific surface area can lead to lower local current densities in a porous substrate, resulting in a denser Li deposition morphology and more efficient pore filling. Therefore, future options for optimizing the deposition morphology in the Cu micro-foam include expanding the specific surface area by adjusting the pore size and porosity. This could also affect the micro-foams' capacity of subsurface Li uptake by increasing the total pore volume and widening the pore necks.

Fig. 4b shows a cryo-FIB-SEM cross-section image of a flat Cu foil with 0.20 mA h cm^{-2} of deposited Li. This allows for comparison of the Li deposition behavior on a 2D current collector to that inside the 3D Cu micro-foam discussed above. The Cu foil shows a more heterogeneous Li deposition morphology consisting of alternating larger and smaller blocks of Li with many voids of different sizes in between. The Li structures on the Cu foil surface appear considerably less dense than those seen for deposition inside the Cu micro-foam material. Compared to the dense Li deposition in the upper part of the Cu micro-foam, a main reason for the heterogeneous deposition behavior on the Cu foil is the higher effective current density. Also, the lack of a guiding structure that could be filled by the depositing Li contributes to the inhomogeneous deposition. When comparing Fig. 4a and b, the Li metal layer deposited on the flat Cu foil is also notably thicker than that on top of the Cu micro-foam (outside the surface pores). Therefore, the Cu foil electrode exhibits a higher volume expansion than the Cu micro-foam after Li electrodeposition equal to 0.20 mA h cm^{-2}. This shows that the Cu micro-foam can considerably reduce the volume expansion by hosting the Li electrodeposition within its pore volume.

Combining the insights from the SEM observations and the current density distribution simulations, the scheme in Fig. 5 represents the proposed growth behavior of Li on the Cu micro-foams under the conditions used in this work. The schematic representation uses a continuous color scheme to visualize the Li electrodeposition: initially appearing structural features are depicted in light green while the subsequent growth of these Li structures is shown in progressively darker shades of blue.

Owing to the wetting of the negative electrode during the resting step after cell assembly, the pore network of the micro-foam is initially filled with electrolyte rich in Li ions. This leads to the formation of homogeneously distributed Li nuclei on all the Cu surfaces at the onset of the deposition current as depicted in Fig. 5a and S1b.† The found increase of the effective current density from the top surfaces to the underlying pores causes "fresh" Li ions to move into the pore network upon their arrival at the negative electrode. Since Li deposition on existing Li structures is preferred over deposition on a Cu surface,[76] the growth of the Li nuclei inside the micro-foam pores is stimulated by the influx of the new Li ions (Fig. S1c and d†). Some of the growing Li nuclei merge with neighboring nuclei and form medium sized structures, which attract further electrodeposition (see Fig. 5b and marking in Fig. S1c†). As the deposition

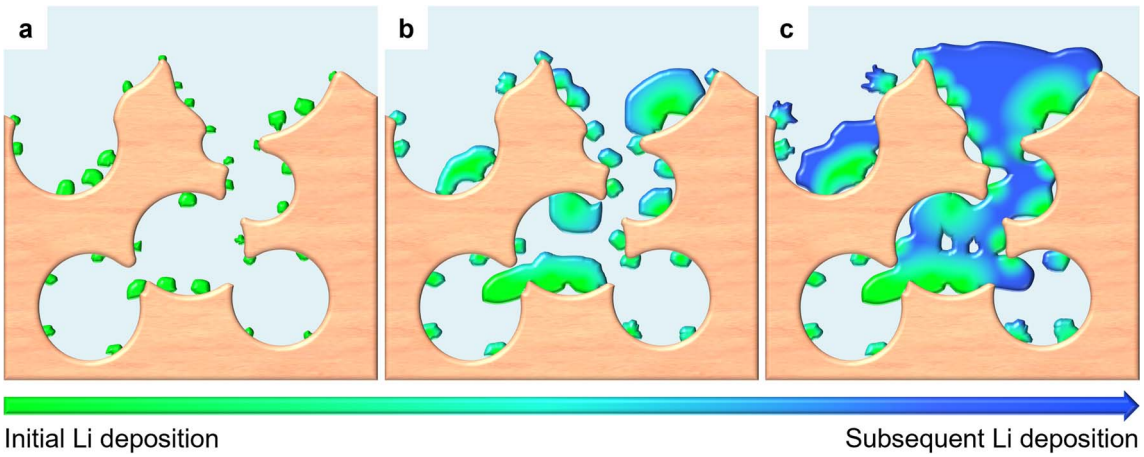

Fig. 5 Schematic representation of the continuous growth of Li structures inside the Cu micro-foam pores during Li electrodeposition at a current density of 0.1 mA cm^{-2}. A continuous color scheme denotes the progressing expansion of the Li structures from (a) initial (green) to (b and c) subsequent (blue) electrodeposits.

progresses, these combined Li electrodeposits grow into large homogeneous deposition structures that store substantial amounts of Li in pores both on and below the substrate surface, filling the free volume of the host material (Fig. 5c).

This deposition behavior explains the observed lower surface coverage of the Cu micro-foams as compared to flat Cu foil. In addition, Fig. S2 (ESI†) shows that the Li structures formed on the Cu micro-foam are denser and more compact than those found on the flat Cu foil. This increase in deposition density is caused by the more distributed effective current density in the upper parts of the Cu micro-foam that reduces HSAL formation. The preferred formation of dense Li structures helps in storing more Li inside the pores of the Cu micro-foam host material, further limiting the areal and volumetric expansion of Li structures on top of the micro-foam. Ultimately, the found deposition behavior proves that the created Cu micro-foams have a beneficial effect on the Li storage at the negative electrode of ZELMBs.

Electrochemical investigations

Comparing the voltage profiles for Li electrodeposition on the 3D Cu micro-foams to those on 2D flat and surface structured dendritic Cu foil (Fig. 6) also shows substantial differences in the Li deposition character. In these profiles, the initial drop to a minimum below 0 V, often referred to as the nucleation overvoltage, represents the activation energy required to start the Li deposition under the given circumstances.[74,77] The nucleation overvoltage depends on various factors including the material of the deposition surface, the surface geometry and morphology, and experimental parameters such as the applied deposition current.[76,77]

Fig. 6a shows that the deposition of Li on a Cu micro-foam at a current density of 0.1 mA cm^{-2} yielded a nucleation overvoltage of 32.6 mV. This value is substantially lower than the nucleation overvoltages measured for Li deposition on flat Cu foil (57.6 mV) and dendritic Cu foil (52.7 mV). An analogous relation was detected for the steady-state Li deposition plateau that is also less negative for the Cu micro-foam as compared to both flat and dendritic Cu foil (inset in Fig. 6a). The main reasons for these observations are the larger active surface area used for deposition in the porous Cu micro-foam and the observed lower effective current density in these regions. These factors are known to homogenize the Li distribution and to minimize dendrite growth tendencies while retaining the same overall deposition rate.[74] The minor surface area enhancement of the dendritic Cu foil does not achieve a substantial decrease of the effective current density over flat Cu foil (see Fig. S4, ESI†). This results in a comparably high nucleation overvoltage for the dendritic foil (similar to that of the flat foil). These results indicate that the morphology of the Cu micro-foam effectively reduces the activation barrier for Li electrodeposition compared to commercial flat and dendritic Cu foils, likely facilitating the formation of more homogeneous Li structures. The observations described above were further validated by monitoring the voltage during Li deposition at a higher current density (0.5 mA cm^{-2}). This yielded similar results (Fig. 6b), implying that the beneficial influence of the porous Cu micro-foam on the Li deposition is independent of the applied current density.

In Fig. 6a and b, the increased surface area of the Cu micro-foam and the dendritic Cu foil also results in a shift of the nucleation overvoltage signals to a later point when more charge has been passed. The reasons for this are extended SEI formation and lithiation of the native oxidic surface layer due to the enhanced surface areas.[12] These processes cause increased charge consumption at cell voltages >0 V before the start of the Li deposition, delaying the completion of the nucleation step.[74] Once again, this effect is more evident for the Cu micro-foam than for the dendritic Cu foil due to the larger active surface area and more pronounced native oxide layer. Consequently,

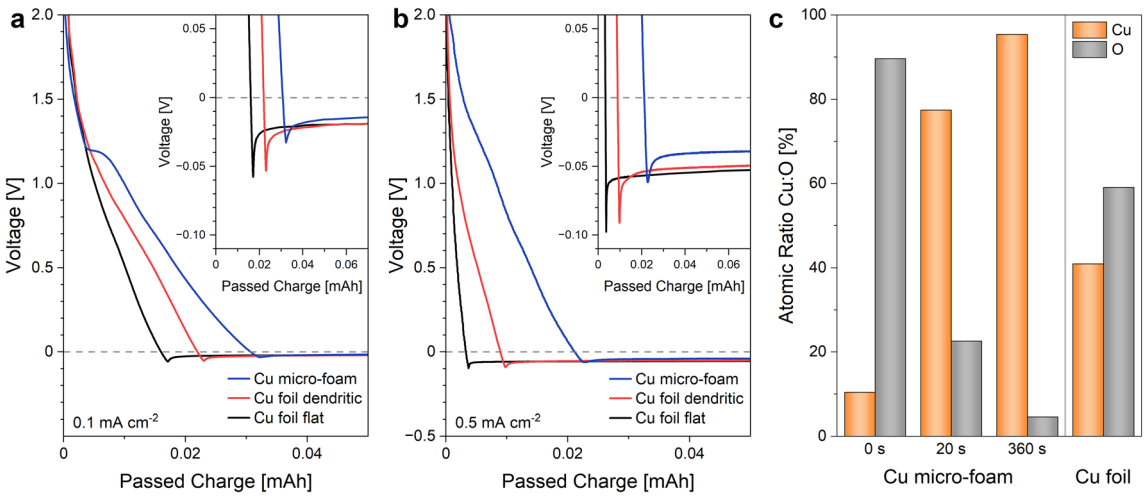

Fig. 6 (a and b) Voltage *vs.* transferred charge profiles acquired during the nucleation and early deposition phase for galvanostatic electrodeposition of Li on flat Cu foil (black), dendritic Cu foil (red), and Cu micro-foam (blue) current collectors. Nominal current density: (a) 0.1 mA cm^{-2} or (b) 0.5 mA cm^{-2} relative to *x*–*y*-plane area of the current collectors. The insets show zoomed-in views of the voltage area relevant for Li nucleation. (c) Atomic ratio between Cu (orange) and O (grey) on the surface of a Cu micro-foam (after various times of Ar^+ sputter depth profiling, denoted in seconds) and flat Cu foil as determined by XPS analysis.

the micro-foam voltage profile in Fig. 6a shows a "shoulder" at 1.2 V representing the SEI formation and surface oxide lithiation while the graphs related to the low surface area Cu foils show just delays in the voltage drop.

To gain further insight about the mentioned surface reactivity of the samples, the composition of the native layers on the created Cu micro-foam and commercial Cu foil was investigated by XPS (Fig. 6c).[78] The found atomic Cu : O ratio of 1 : 8.65 indicates that the pristine Cu micro-foam surface layer is highly oxidized, which presumably results from side reactions with the aqueous electrodeposition electrolyte and ambient air. In contrast, the commercial 2D Cu foil shows a Cu : O ratio of 1 : 1.44, indicating a higher Cu content and less oxidic nature of the surface layer. The detected higher proportion of O on the Cu micro-foam surface confirms that more Li will be lost due to lithiation processes when the charging current is applied.[12,79] Also, the elemental composition of deeper layers of the Cu micro-foam was investigated through sputter depth profiling (SDP) with an Ar^+-beam. The Cu : O ratio increased to 3.44 : 1 after 20 s of sputtering, and a ratio of 20.65 : 1 was found after a total sputtering time of 320 s. These results confirm that the bulk material of the prepared Cu micro-foam consists mostly of metallic Cu buried beneath a thin oxidic surface layer.[78,79] Although the capacity consumed during the lithiation of the oxidic layer is low, removal of the oxidic species by diluted acid washing or reductive annealing[80] could be considered as a post treatment after the Cu micro-foam synthesis. However, since oxidic surface layers on Cu were also shown to improve certain Li storage properties,[12,81] further research is required to assess the usefulness of removing the surface oxides.

The electrochemical charge/discharge cycling behavior of Cu micro-foam ZELMB cells with NCA-based positive electrodes further highlights the influence of the substrate for Li deposition. Fig. 7 shows a comparison between the long-term cycling results of ZELMB cells using Cu micro-foams, flat Cu foil, or dendritic Cu foil as the negative electrode. As displayed in Fig. 7a, the cells with a Cu micro-foam negative electrode show a CE of 86.3% during the first cycle, which is lower than the initial CE values of 91.6% and 89.6% for the cells with plain and dendritic Cu foil. The larger effective surface area and the pronouncedly oxidized surface layer of the Cu micro-foams lead to notably more SEI formation and oxide lithiation during the initial Li nucleation as discussed above. This results in slightly higher initial discharge capacities for the Cu foil cells as shown in Fig. 7b.

Due to these side reactions, the cell voltage curve for the first Li deposition in the Cu micro-foam (Fig. 7c) shows a certain charge consumption at voltages <4 V before the onset of Li metal deposition. Fig. 7d shows that this effect is present to a lower extent for a cell with dendritic Cu foil; however, such behavior is not noticeable for the cell with plain Cu foil due to the small surface area (Fig. 7e). Comparing Fig. 7c–e shows that the difference between first cycle charge (similar for all cells) and discharge capacity, that is mainly attributed to SEI formation and oxidic surface layer lithiation, consists of two parts: (I) an amount of charge similar for all three current collectors is lost to the surface layer formation on the depositing Li metal, and (II) an additional charge portion is spent for electrolyte decomposition and oxide layer lithiation on the Cu substrate before the Li nucleation. This second increment of charge loss is considerable for the Cu micro-foam (represented by the "shoulder" in Fig. 7c, see also Fig. 6) while it is minor for the dendritic Cu foil and nearly irrelevant for the flat Cu foil. This difference highlights the direct influence of the deposition substrates' surface area on the Li loss during the first cycle. In addition, the reversible trapping of a certain amount of Li in the

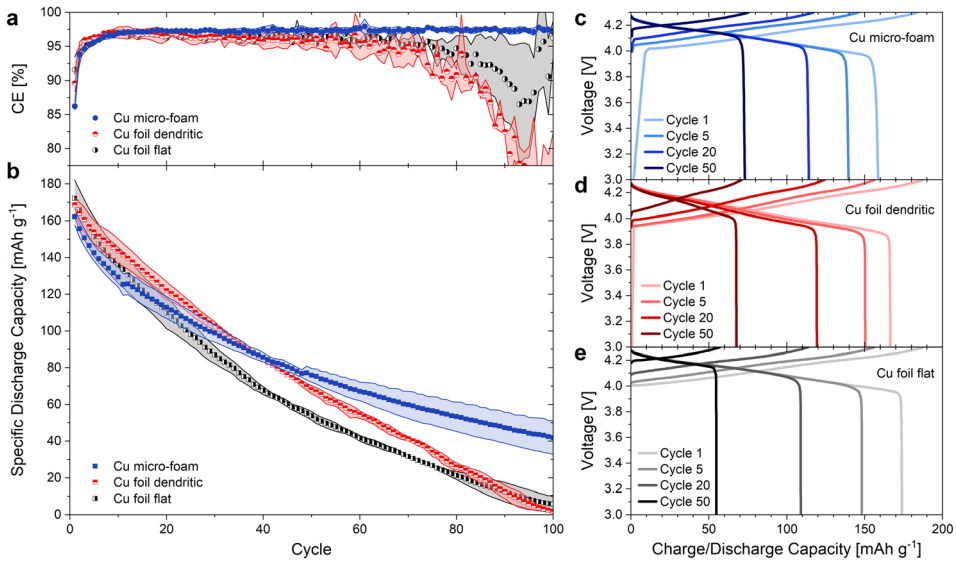

Fig. 7 (a) Coulombic efficiency and (b) average discharge capacity measured when charge/discharge cycling NCA||Cu micro-foam (blue), NCA||Cu foil dendritic (red), and NCA||Cu foil flat (black) cells with a current density of 0.2 mA cm^{-2} (0.2C) for 100 cycles at 40 °C. The results of three equivalent cells are averaged for every set-up. Corresponding charge/discharge voltage profiles for cells with (c) Cu micro-foam, (d) dendritic Cu foil, and (e) flat Cu foil negative electrodes.

micro-foam pores may contribute to the reduced initial discharge capacity. Yet, reactivation of this trapped Li might be possible upon further cycling.

The capacity retention rates and CE values continuously increase for all investigated current collector types as the SEI formation progresses over the next few cycles. From the tenth cycle onwards, the Cu micro-foam-based cells display a remarkably stable CE that is constantly above 97%. In contrast, the cells with flat and dendritic Cu foil show lower and more fluctuating CEs that get continuously less stable upon prolonged charge/discharge cycling. Adding up the coulombic inefficiency for each cycle shows that the cells with Cu micro-foams, flat Cu foil, and dendritic Cu foil accumulate 289.6%, 485.6%, and 764.1% of coulombic inefficiency over the course of 100 cycles, respectively (Fig. S5, ESI†). This means that the extraction of Li from the micro-foam current collectors during discharge is substantially more efficient compared to the cells with Cu foil electrodes.

Resulting from the increased capacity retention, the Cu micro-foam cells show a slower capacity decay after the tenth cycle. The remaining discharge capacity of the micro-foam-based cells surpasses that of the cells with flat and dendritic Cu foil starting from cycles 20 and 40, respectively. After cycle 70, the declining and erratic CE curves of the cells with flat and dendritic Cu foil indicate formation of Li dendrites. After 100 cycles, the Cu micro-foam-based cells still retain a discharge capacity of 42 ± 9 mA h g^{-1} (22.3% $\pm$ 4.8% capacity retention). At the same point in time, the cells with flat Cu foil and dendritic Cu foil show negligible remaining discharge capacities of 6 mA h $g^{-1} \pm 5$ mA h g^{-1} (3.2% $\pm$ 2.7% capacity retention) and 2 mA h $g^{-1} \pm 1$ mA h g^{-1} (1.1% $\pm$ 0.5% capacity retention), respectively.

As discussed above, an important reason for the higher CE and capacity retention values of the Cu micro-foam cells is the lower effective current density in the upper part of the micro-foam that enables denser Li deposition on and in the host structure. Also, the porous structure offers defined deposition spaces that remain constant instead of changing after each cycle. Apparently, the pores are reversibly filled and emptied during electrochemical deposition and dissolution of Li, which limits continuous SEI formation on newly exposed Li surfaces. Also, the Li structures inside the micro-foam pores are surrounded by conductive surfaces, thus they are in better contact to their current collector than Li deposited on 2D Cu foil. Therefore, the Li in the Cu micro-foams is less likely to transition to "dead" Li by losing electronic contact to the current collector. Also, formed "dead" Li can presumably remain trapped in the pores, allowing for reconnection to the electrode during subsequent deposition phases. Furthermore, minimized HSAL formation and limited electrolyte contact of the Li in the pores reduce the amount of side reactions occurring on Li surfaces, contributing to the improved Li inventory preservation.

The presented liquid electrolyte-based ZELMB set-up could deliver practical stack level specific energy and energy density values of 249 W h kg^{-1} and 783 W h L^{-1}, respectively. This implies usage of the prepared Cu micro-foam (thickness approximately 52.2 μm) on a thin Cu foil base layer (thickness 5 μm) as the negative electrode, an NCA-based positive electrode, and pore-filling amounts of electrolyte (details in Table S1†). Furthermore, employing a Cu micro-foam with a reduced thickness of 15 μm in an otherwise unchanged ZELMB cell would save weight and volume, increasing the stack level specific energy and energy density to 351 W h kg^{-1} and 1087 W h L^{-1}, respectively. Such ZELMB cells can deliver a notably higher energy density and maintain a similar specific energy compared to LMBs with Li metal based negative electrodes that carry a substantial Li excess. Using Cu micro-foams with the optimized thickness of 15 μm would also improve the agreement between the total Li uptake capacity of the micro-foam (2.20 mA h cm^{-2}) and the amount of Li that can be supplied by commonly used positive electrodes.

Together with the presented improvements in cycle life and capacity retention, the high practical specific energy and energy density values underline the significance of 3D structured current collectors like the Cu micro-foams for ZELMBs. Combining the usage of the Cu micro-foam negative electrodes with the implementation of further optimization approaches will likely lead to the creation of long-lasting high performance ZELMB cells in future studies. Also, due to the increased cycling stability, ZELMBs utilizing the created Cu micro-foams represent a favorable set-up for the analysis of electrochemical deposition and dissolution processes.[18]

Conclusion

This work thoroughly investigated the Li deposition behavior in ZELMB cells with open-porous 3D Cu micro-foam current collectors that were prepared *via* an optimized templated electrodeposition process. For the first time in a ZELMB, the details of internal pore filling during Li deposition were revealed using *ex situ* SEM mapping of surfaces and cross-sections, Li-sensitive *in situ* cryo-FIB-SEM imaging, current density distribution simulations, electrochemical investigations, and XPS analysis. Tracing the Li deposition behavior from nucleation to large-scale deposition, this work showed that the open-porous network structure of the Cu micro-foams can store substantial amounts of Li in surface and sub-surface pores in a dense and compact morphology. This reduces HSAL growth, volume fluctuations, "dead" Lithium formation, and detrimental side reactions, thereby avoiding many characteristic problems for Li cycling on flat current collectors.

The Cu micro-foam's large surface area causes a lower effective current density in the upper region of the porous material, reducing the nucleation overvoltage for Li deposition by $\approx$40% compared to both flat and dendritic Cu foil. In ZELMBs with NCA-based positive electrodes, Cu micro-foam negative electrodes enabled a high coulombic efficiency (constantly above 97%), increased capacity retention, and prolonged cycle life compared to cells with flat and dendritic Cu foil negative electrodes. This highlights that 3D current collectors like the presented Cu micro-foam can be an important building block for future application-ready ZELMBs. Also, ZELMB cells with a Cu micro-foam negative electrode can be used as a stable

model system to investigate electrochemical Li deposition and dissolution.

Author contributions

T. T. K. I.: conceptualization (main), data curation (main), formal analysis (main), investigation (main), methodology (main), validation (main), visualization (main), writing – original draft (main), writing – review & editing (main); M. M. B.: data curation (supporting), investigation (supporting), methodology (supporting), writing – original draft (supporting), writing – review & editing (supporting); F. P.: formal Analysis (equal), methodology (supporting), writing – original draft (supporting), writing – review & editing (supporting); J. F. D.: data curation (supporting), investigation (supporting), writing – original draft (supporting), writing – review & editing (supporting); P. B.: funding acquisition (supporting), supervision (supporting), project administration (equal), resources (main), writing – review & editing (supporting); M. B.: conceptualization (supporting), funding acquisition (supporting), project administration (supporting), supervision (supporting), writing – original draft (supporting), writing – review & editing (equal); M. W.: conceptualization (supporting), funding acquisition (main), project administration (main), supervision (main), writing – original draft (supporting), writing – review & editing (equal); M. C. S.: conceptualization (supporting), funding acquisition (supporting), supervision (supporting), visualization (supporting), writing – original draft (supporting), writing – review & editing (equal).

Conflicts of interest

There are no conflicts to declare.

Acknowledgements

Financial support provided by the German Federal Ministry of Education and Research (BMBF) within the research projects "MEET Hi-EnD III" (03XP0258A), "ProLiFest" (03XP0253A), and "AMaLiS" (03XP0125D) is gratefully acknowledged.

References

1 M. Winter, B. Barnett and K. Xu, *Chem. Rev.*, 2018, **118**, 11433.
2 W. Liu, T. Placke and K. T. Chau, *Energy Rep.*, 2022, **8**, 4058.
3 M. Marinaro, D. Bresser, E. Beyer, P. Faguy, K. Hosoi, H. Li, J. Sakovica, K. Amine, M. Wohlfahrt-Mehrens and S. Passerini, *J. Power Sources*, 2020, **459**, 228073.
4 R. Schmuch, R. Wagner, G. Hörpel, T. Placke and M. Winter, *Nat. Energy*, 2018, **3**, 267.
5 D. Malka, R. Attias, N. Shpigel, F. Malchick, M. D. Levi and D. Aurbach, *Isr. J. Chem.*, 2021, **61**, 11.
6 G. M. Hobold, J. Lopez, R. Guo, N. Minafra, A. Banerjee, Y. Shirley Meng, Y. Shao-Horn and B. M. Gallant, *Nat. Energy*, 2021, **6**, 951.
7 J.-G. Zhang, W. Xu, J. Xiao, X. Cao and J. Liu, *Chem. Rev.*, 2020, **120**, 13312.
8 Y. Zhang, T.-T. Zuo, J. Popovic, K. Lim, Y.-X. Yin, J. Maier and Y.-G. Guo, *Mater. Today*, 2020, **33**, 56.
9 X. He, D. Bresser, S. Passerini, F. Baakes, U. Krewer, J. Lopez, C. T. Mallia, Y. Shao-Horn, I. Cekic-Laskovic, S. Wiemers-Meyer, F. A. Soto, V. Ponce, J. M. Seminario, P. B. Balbuena, H. Jia, W. Xu, Y. Xu, C. Wang, B. Horstmann, R. Amine, C.-C. Su, J. Shi, K. Amine, M. Winter, A. Latz and R. Kostecki, *Nat. Rev. Mater.*, 2021, **6**, 1036.
10 C. Heubner, S. Maletti, H. Auer, J. Hüttl, K. Voigt, O. Lohrberg, K. Nikolowski, M. Partsch and A. Michaelis, *Adv. Funct. Mater.*, 2021, 2106608.
11 Y. Ren, Z. Cui, A. Bhargav, J. He and A. Manthiram, *Adv. Funct. Mater.*, 2022, **32**, 2106680.
12 K. Schönherr, B. Schumm, F. Hippauf, R. Lissy, H. Althues, C. Leyens and S. Kaskel, *Chem. Eng. J. Adv.*, 2022, **9**, 100218.
13 C. Niu, D. Liu, J. A. Lochala, C. S. Anderson, X. Cao, M. E. Gross, W. Xu, J.-G. Zhang, M. S. Whittingham, J. Xiao and J. Liu, *Nat. Energy*, 2021, **6**, 723.
14 P. Shi, X.-B. Cheng, T. Li, R. Zhang, H. Liu, C. Yan, X.-Q. Zhang, J.-Q. Huang and Q. Zhang, *Adv. Mater.*, 2019, **31**, 1902785.
15 B. J. Neudecker, N. J. Dudney and J. B. Bates, *J. Electrochem. Soc.*, 2000, **147**, 517.
16 O. Lohrberg, S. Maletti, C. Heubner, M. Schneider and A. Michaelis, *J. Electrochem. Soc.*, 2022, **169**, 30543.
17 Z. Xie, Z. Wu, X. An, X. Yue, J. Wang, A. Abudula and G. Guan, *Energy Storage Mater.*, 2020, **32**, 386.
18 M. Genovese, A. J. Louli, R. Weber, S. Hames and J. R. Dahn, *J. Electrochem. Soc.*, 2018, **165**, A3321.
19 E. Kazyak, M. J. Wang, K. Lee, S. Yadavalli, A. J. Sanchez, M. D. Thouless, J. Sakamoto and N. P. Dasgupta, *Matter*, 2022, **5**, 3912.
20 J. Qian, B. D. Adams, J. Zheng, W. Xu, W. A. Henderson, J. Wang, M. E. Bowden, S. Xu, J. Hu and J.-G. Zhang, *Adv. Funct. Mater.*, 2016, **26**, 7094.
21 C.-J. Huang, B. Thirumalraj, H.-C. Tao, K. N. Shitaw, H. Sutiono, T. T. Hagos, T. T. Beyene, L.-M. Kuo, C.-C. Wang, S.-H. Wu, W.-N. Su and B.-J. Hwang, *Nat. Commun.*, 2021, **12**, 1.
22 Z. Tong, B. Bazri, S.-F. Hu and R.-S. Liu, *J. Mater. Chem. A*, 2021, **9**, 7396.
23 S. Nanda, A. Gupta and A. Manthiram, *Adv. Energy Mater.*, 2020, **11**, 2000804.
24 A. J. Louli, M. Coon, M. Genovese, J. deGooyer, A. Eldesoky and J. R. Dahn, *J. Electrochem. Soc.*, 2021, **168**, 20515.
25 J. Chen, B. He, Z. Cheng, Z. Rao, D. He, D. Liu, X. Li, L. Yuan, Y. Huang and Z. Li, *J. Electrochem. Soc.*, 2021, **168**, 120535.
26 G. Bieker, M. Winter and P. Bieker, *Phys. Chem. Chem. Phys.*, 2015, **17**, 8670.
27 A. A. Assegie, J.-H. Cheng, L.-M. Kuo, W.-N. Su and B.-J. Hwang, *Nanoscale*, 2018, **10**, 6125.
28 S. Sheng, L. Sheng, L. Wang, N. Piao and X. He, *J. Power Sources*, 2020, **476**, 228749.

29 J. Chen, Q. Li, T. P. Pollard, X. Fan, O. Borodin and C. Wang, *Mater. Today*, 2020, **39**, 118.
30 A. Eldesoky, A. J. Louli, A. Benson and J. R. Dahn, *J. Electrochem. Soc.*, 2021, **168**, 120508.
31 T. M. Hagos, G. B. Berhe, T. T. Hagos, H. K. Bezabh, L. H. Abrha, T. T. Beyene, C.-J. Huang, Y.-W. Yang, W.-N. Su, H. Dai and B.-J. Hwang, *Electrochim. Acta*, 2019, **316**, 52.
32 T. T. Hagos, B. Thirumalraj, C.-J. Huang, L. H. Abrha, T. M. Hagos, G. B. Berhe, H. K. Bezabh, J. Cherng, S.-F. Chiu, W.-N. Su and B.-J. Hwang, *ACS Appl. Mater. Interfaces*, 2019, **11**, 9955.
33 B. A. Jote, T. T. Beyene, N. A. Sahalie, M. A. Weret, B. W. Olbassa, Z. T. Wondimkun, G. B. Berhe, C.-J. Huang, W.-N. Su and B. J. Hwang, *J. Power Sources*, 2020, **461**, 228102.
34 R. Weber, M. Genovese, A. J. Louli, S. Hames, C. Martin, I. G. Hill and J. R. Dahn, *Nat. Energy*, 2019, **4**, 683.
35 T. T. K. Ingber, D. Liebenau, M. Biedermann, M. Kolek, D. Diddens, H.-D. Wiemhöfer, A. Heuer, M. Winter and P. Bieker, *J. Electrochem. Soc.*, 2021, **168**, 70559.
36 Y.-H. Lin, C.-Y. Shih, R. Subramani, Y.-L. Lee, J.-S. Jan, C.-C. Chiu and H. Teng, *J. Mater. Chem. A*, 2022, **10**, 4895.
37 Z. Yu, H. Wang, X. Kong, W. Huang, Y. Tsao, D. G. Mackanic, K. Wang, X. Wang, W. Huang, S. Choudhury, Y. Zheng, C. V. Amanchukwu, S. T. Hung, Y. Ma, E. G. Lomeli, J. Qin, Y. Cui and Z. Bao, *Nat. Energy*, 2020, **4**, 893.
38 M. Genovese, A. J. Louli, R. Weber, C. Martin, T. Taskovic and J. R. Dahn, *J. Electrochem. Soc.*, 2019, **166**, A3342.
39 L. Lin, L. Suo, Y. Hu, H. Li, X. Huang and L. Chen, *Adv. Energy Mater.*, 2021, **11**, 2003709.
40 S. Koul, Y. Morita, F. Fujisaki, H. Ogasa, Y. Fujiwara and A. Kushima, *J. Electrochem. Soc.*, 2022, **169**, 20542.
41 S. S. Zhang, X. Fan and C. Wang, *Electrochim. Acta*, 2017, **258**, 1201.
42 B. Zhou, A. Bonakdarpour, I. Stoševski, B. Fang and D. P. Wilkinson, *Prog. Mater. Sci.*, 2022, **130**, 100996.
43 A. A. Assegie, C.-C. Chung, M.-C. Tsai, W.-N. Su, C.-W. Chen and B.-J. Hwang, *Nanoscale*, 2019, **11**, 2710.
44 J. Jung, J. Y. Kim, I. J. Kim, H. Kwon, G. Kim, G. Doo, W. Jo, H.-T. Jung and H.-T. Kim, *J. Mater. Chem. A*, 2022, **10**, 20984.
45 Z. Zhang, H. Luo, Z. Liu, S. Wang, X. Zhou and Z. Liu, *J. Mater. Chem. A*, 2022, **10**, 9670.
46 O. Lohrberg, K. Voigt, S. Maletti, H. Auer, K. Nikolowski, C. Heubner and A. Michaelis, *Adv. Funct. Mater.*, 2023, **33**, 2214891.
47 P. Liang, H. Sun, C.-L. Huang, G. Zhu, H.-C. Tai, J. Li, F. Wang, Y. Wang, C.-J. Huang, S.-K. Jiang, M.-C. Lin, Y.-Y. Li, B.-J. Hwang, C.-A. Wang and H. Dai, *Adv. Mater.*, 2022, **34**, e2207361.
48 Q. Li, S. Zhu and Y. Lu, *Adv. Funct. Mater.*, 2017, **27**, 1606422.
49 D. Yin, G. Huang, S. Wang, D. Yuan, X. Wang, Q. Li, Q. Sun, H. Xue, L. Wang and J. Ming, *J. Mater. Chem. A*, 2020, **8**, 1425.
50 K.-H. Chen, A. J. Sanchez, E. Kazyak, A. L. Davis and N. P. Dasgupta, *Adv. Energy Mater.*, 2019, **9**, 1802534.
51 K. Chen, R. Pathak, A. Gurung, K. M. Reza, N. Ghimire, J. Pokharel, A. Baniya, W. He, J. J. Wu, Q. Qiao and Y. Zhou, *J. Mater. Chem. A*, 2020, **8**, 1911.
52 X. Wang, G. Pawar, Y. Li, X. Ren, M. Zhang, B. Lu, A. Banerjee, P. Liu, E. J. Dufek, J.-G. Zhang, J. Xiao, J. Liu, Y. S. Meng and B. Liaw, *Nat. Mater.*, 2020, **19**, 1339.
53 B. Yoon, J. Park, J. Lee, S. Kim, X. Ren, Y. M. Lee, H.-T. Kim, H. Lee and M.-H. Ryou, *ACS Appl. Mater. Interfaces*, 2019, **11**, 31777.
54 X. Zhang, Z. Chen, L. Shui, C. Shang, X. Wang and G. Zhou, *Nanoscale Adv.*, 2019, **1**, 527.
55 H. Zhang, J. Yang, H. Hou, S. Chen and H. Yao, *Sci. Rep.*, 2017, **7**, 7769.
56 M. Yao, K. Okuno, T. Iwaki, M. Kato, S. Tanase, K. Emura and T. Sakai, *J. Power Sources*, 2007, **173**, 545.
57 G.-F. Yang and S.-K. Joo, *Electrochim. Acta*, 2015, **170**, 263.
58 H. Liu, E. Wang, Q. Zhang, Y. Ren, X. Guo, L. Wang, G. Li and H. Yu, *Energy Storage Mater.*, 2019, **17**, 253.
59 F. Heim, T. Kreher and K. P. Birke, *Batteries*, 2020, **6**, 20.
60 G. H. Lee, J. W. Lee, J. I. L. Choi, S. J. Kim, Y.-H. Kim and J. K. Kang, *Adv. Funct. Mater.*, 2016, **26**, 5139.
61 G. Hu, C. Xu, Z. Sun, S. Wang, H.-M. Cheng, F. Li and W. Ren, *Adv. Mater.*, 2016, **28**, 1603.
62 N. Issatayev, A. Nuspeissova, G. Kalimuldina and Z. Bakenov, *J. Power Sources Adv.*, 2021, **10**, 100065.
63 T. T. H. Hoang, S. Ma, J. I. Gold, P. J. A. Kenis and A. A. Gewirth, *ACS Catal.*, 2017, **7**, 3313.
64 H. N. Umh, J. Park, J. Yeo, S. Jung, I. Nam and J. Yi, *Electrochem. Commun.*, 2019, **99**, 27.
65 H. Liu, X. Yue, X. Xing, Q. Yan, J. Huang, V. Petrova, H. Zhou and P. Liu, *Energy Storage Mater.*, 2019, **16**, 505.
66 C. Wang, M. Liu, M. Thijs, F. G. B. Ooms, S. Ganapathy and M. Wagemaker, *Nat. Commun.*, 2021, **12**, 6536.
67 M. Zatorska, G. Łazarski, U. Maziarz, N. Wilkosz, T. Honda, S.-I. Yusa, J. Bednar, D. Jamróz and M. Kepczynski, *Int. J. Pharm.*, 2020, **591**, 120031.
68 R. Jalil and J. R. Nixon, *J. Microencapsulation*, 1990, **7**, 297.
69 P. B. O'Donnell and J. W. McGinity, *Adv. Drug Delivery Rev.*, 1997, **28**, 25.
70 C. Zhang, J. W. Palko, G. Rong, K. S. Pringle, M. T. Barako, T. J. Dusseault, M. Asheghi, J. G. Santiago and K. E. Goodson, *ACS Appl. Mater. Interfaces*, 2018, **10**, 30487.
71 B. T. Holland, C. F. Blanford, T. Do and A. Stein, *Chem. Mater.*, 1999, **11**, 795.
72 T. J. Dusseault, J. Gires, M. T. Barako, Y. Won, D. D. Agonafer, M. Asheghi, J. G. Santiago and K. E. Goodson, in *Proceedings of the Fourteenth Intersociety Conference on Thermal and Thermomechanical Phenomena in Electronic Systems (ITherm)*, IEEE, Piscataway, NJ, 2014, pp. 750–755.
73 N. Fairley, V. Fernandez, M. Richard-Plouet, C. Guillot-Deudon, J. Walton, E. Smith, D. Flahaut, M. Greiner, M. Biesinger, S. Tougaard, D. Morgan and J. Baltrusaitis, *Appl. Surf. Sci. Adv.*, 2021, **5**, 100112.
74 A. Pei, G. Zheng, F. Shi, Y. Li and Y. Cui, *Nano Lett.*, 2017, **17**, 1132.

75 Q. Yun, Y.-B. He, W. Lv, Y. Zhao, B. Li, F. Kang and Q.-H. Yang, *Adv. Mater.*, 2016, **28**, 6932.
76 V. Pande and V. Viswanathan, *ACS Energy Lett.*, 2019, **4**, 2952.
77 N. Xu, L. Li, Y. He, Y. Tong and Y. Lu, *J. Mater. Chem. A*, 2020, **8**, 6229.
78 P. Niehoff, S. Passerini and M. Winter, *Langmuir*, 2013, **29**, 5806.
79 H. Bubert, E. Grallath, A. Quentmeier, M. Wielunski and L. Borucki, *Fresenius. J. Anal. Chem.*, 1995, **353**, 456.
80 L.-L. Lu, J. Ge, J.-N. Yang, S.-M. Chen, H.-B. Yao, F. Zhou and S.-H. Yu, *Nano Lett.*, 2016, **16**, 4431.
81 J. Chen, L. Dai, P. Hu and Z. Li, *Molecules*, 2023, 28.